Journal of the Korean Physical Society, Vol. 55, No. 4, October 2009, pp. 1451∼1460

Phase-field Model for the Pinchoff of Liquid-liquid Jets

Chang-Hun KIM* and Seung-Ho SHIN†
Department of Computer Science, Korea University, Seoul 136-701

Hyun Geun LEE‡ and Junseok KIM§
Department of Mathematics, Korea University, Seoul 136-701

(Received 22 December 2008)

Understanding pinchoff in a liquid-liquid jet is one of the fundamental problems in the physics of fluid. Pinchoff has a wide variety of applications, such as in ink-jet printers. We have need a phase-field model to numerically investigate the breakup of a forced liquid jet into drops in immiscible liquid-liquid systems. In the phase-field model, the classical sharp interface between the two immiscible fluids is represented by a transition region of small, but finite, width. Across this width the composition of one of the two fluids changes continuously. The phase-field method can deal with topological transitions, such as breakup and reconnection, smoothly without ad-hoc "cut and connect" or smoothing procedures. We found the numerical results for the pinchoff of liquid-liquid jets with surface tension to be in good agreement with experimental data. In particular, we investigated the axial velocities and the vorticity structures around the jet neck before and after pinchoff.

PACS numbers: 47.10.ad, 02.70.Bf, 47.11.Bc
Keywords: Liquid jet, Pinchoff, Navier-Stokes equation, Cahn-Hilliard equation, Finite difference method, Projection method, Phase-field method
DOI: 10.3938/jkps.55.1451

I. INTRODUCTION

Free boundary problems represent excellent approximations to a number of important engineering, industrial, and biomedical problems such as breakup of a liquid column surrounded by another fluid [1]. However, one of the great difficulties in the study of two immiscible fluid flows is the presence of an interface. The interface changes and may undergo severe topological deformations, such as breakup and merging.

The phase-field model [2] provides a natural way of capturing the evolution of complex interfaces and treating the topological changes of the interface. In this model, a mass concentration field $c(\mathbf{x}, t)$ is introduced to denote the mass fraction of one of the components in a heterogeneous mixture of two fluids. The mass concentration is coupled to the fluid motion through a concentration-dependent density, viscosity, and surface tension force. The resulting system couples the Navier-Stokes equations to a fourth-order, degenerate, nonlinear parabolic diffusion equation of the Cahn-Hilliard type for the concentration. The advantages of this approaches are as follows: (1) Topological changes, such as the interface merging and breakup, can be treated without difficulty. (2) The phase field has physical meanings not only on the interface but also in the bulk phases. Therefore, this method can be applied to many physical applications. (3) This method can be straightforwardly extended to a three-dimensional multicomponent system. There are other approaches, such as the lattice Boltzmann method [3, 4], to study multiphase flow [5]. Anderson, McFadden, and Wheeler have authored a review paper of this phase-field model [6].

This paper is organized in the following manner. The definition and the formulation of the governing equation in cylindrical coordinates for the solution to the problem of a Newtonian liquid jet injected vertically into another Newtonian quiescent liquid are introduced in Sec. II. We describe a numerical method in Sec. III. We compare the numerical experiments with available experimental data from Milosevic and Longmire [1] in Sec. IV. Finally, we present conclusions in Sec. V.

II. PROBLEM DEFINITION AND FORMULATION

In this paper, we consider a liquid-liquid jet that pinches off, making droplets. The experimental setup,

*E-mail: chkim@korea.ac.kr;
†E-mail: winstorm@korea.ac.kr;
‡E-mail: leeh@korea.ac.kr;
§E-mail: cfdkim@korea.ac.kr; Fax: +82-2-929-8562

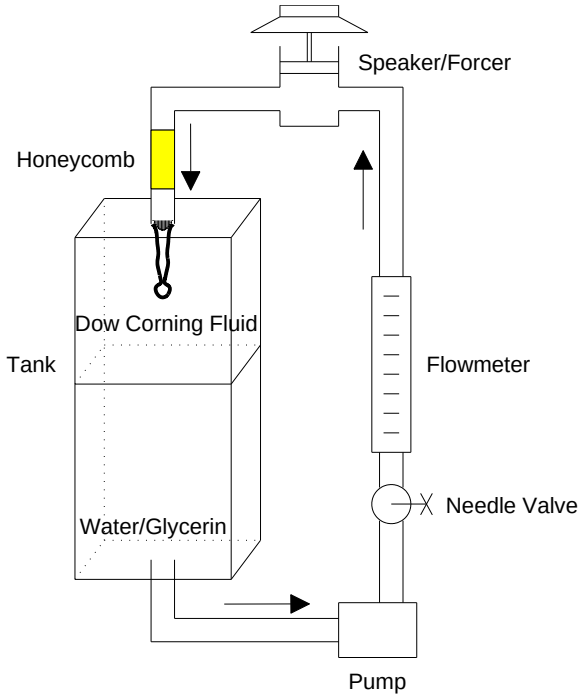

Fig. 1. Recirculating jet facility.

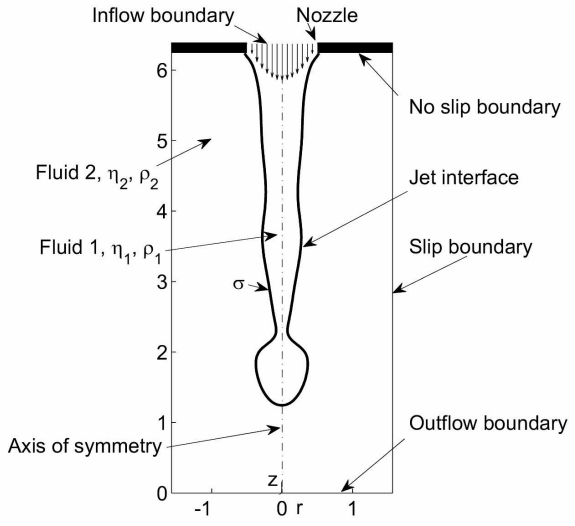

Fig. 2. Liquid/liquid jet flow configuration.

consisting of a tank, a pump, a control valve, a rotameter, and a forcing apparatus, is illustrated in Fig. 1. The dimensions of the tank are $20.3 \times 20.3 \times 56$ cm^3. A magnetic-driven pump generates a steady flow controlled by a needle valve. The flow (a water/glycerin mixture) passes through a honeycomb straightener before exiting a nozzle into an ambient layer of the Dow Corning fluid. More details about the experimental setup are in Ref. 1. The flow configuration investigated numerically in our study is shown in Fig. 2. The jet of a viscous fluid, fluid 1, is injected vertically from a circular nozzle downwards into a tank of a stationary mutually saturated immiscible fluid, fluid 2. The viscosity and the density of the inner jet, fluid 1, are denoted by η_1 and ρ_1, respectively. Likewise, those of the outer ambient, fluid 2, are denoted by η_2 and ρ_2, respectively. The domain is axisymmetric with the center line being the axis of symmetry.

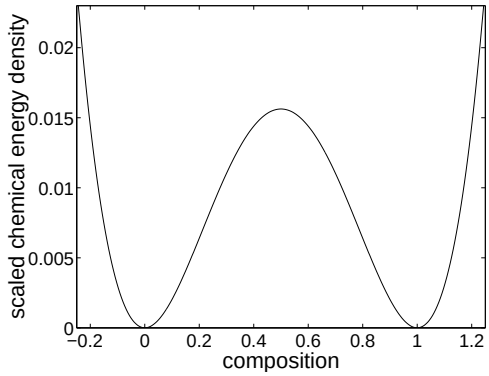

Fig. 3. Double well potential, $F(c) = 0.25c^2(c-1)^2$.

1. The Governing Equations

We consider a situation of a binary fluid consisting of two components, fluid 1 and fluid 2. We denote the composition of component 1, expressed as a mass fraction, by $c(\mathbf{x}, t)$, where $\mathbf{x}$ is the space position and t is the time. In this setting, the composition plays the role of an order parameter that distinguishes the different phases of the fluid. Then, in dimensional form, the phase-field model [7] is

$$\nabla \cdot \mathbf{u} = 0, \tag{1}$$

$$\rho \dot{\mathbf{u}} = -\nabla p + \nabla \cdot [\eta(c)(\nabla \mathbf{u} + \nabla \mathbf{u}^T)] - 6\sqrt{2}\epsilon\sigma \nabla \cdot \left(\frac{\nabla c}{|\nabla c|} \right) |\nabla c| \nabla c + \rho \mathbf{g}, \tag{2}$$

$$\dot{c} = \nabla \cdot (M(c) \nabla \mu), \tag{3}$$

$$\mu = f(c) - \epsilon^2 \Delta c, \tag{4}$$

where $\dot{\cdot} = \partial_t + \mathbf{u} \cdot \nabla$ is the total derivative, $\mathbf{u}$ is the velocity, p is the pressure, $\rho(c) = \rho_1 c + \rho_2(1-c)$ is the density, and $\eta(c) = \eta_1 c + \eta_2(1-c)$ is the viscosity. $-6\sqrt{2}\epsilon\sigma \nabla \cdot \left(\frac{\nabla c}{|\nabla c|} \right) |\nabla c| \nabla c$ is the interfacial tension body force concentrated on the interface, where σ is the interfacial tension coefficient, and ϵ is the interface thickness parameter. $M(c) = Mc(1-c)$ is the variable mobility, μ is the generalized chemical potential, and $f(c) = F'(c)$. $F(c)$ is the Helmholtz free energy, where $F(c) = \frac{1}{4}c^2(1-c)^2$ (see Fig. 3).

2. The Nondimensional Governing Equations

The next step is to restate the dimensional phase-field model in dimensionless form. For this purpose, we de-

fine characteristic values, such as length (L_*), velocity (V_*), viscosity (η_*), density (ρ_*), chemical potential (μ_*), and mobility (M_*). We then introduce non-dimensional variables for the space coordinates, time, velocity components, viscosity, fluid pressure, interface thickness, chemical potential, and mobility:

$$\bar{x} = \frac{x}{L_*}, \quad \bar{\mathbf{u}} = \frac{\mathbf{u}}{V_*}, \quad \bar{\eta} = \frac{\eta}{\eta_*}, \quad \bar{p} = \frac{p}{\rho_* V_*^2},$$
$$\bar{\epsilon} = \frac{\epsilon}{L_*}, \quad \bar{\mu} = \frac{\mu}{\mu_*}, \quad \bar{M} = \frac{M}{M_*},$$

where the bars denote dimensionless variables. Substituting these variables into the governing equations (1)-(4), dropping the bar notations, and using the dimensionless numbers yield the following nondimensional system:

$$\nabla \cdot \mathbf{u} = 0, \tag{5}$$

$$\mathbf{u}_t + \mathbf{u} \cdot \nabla \mathbf{u} = -\nabla p + \frac{1}{Re} \nabla \cdot [\eta(c)(\nabla \mathbf{u} + \nabla \mathbf{u}^T)] \tag{6}$$
$$-\frac{6\sqrt{2}\epsilon}{We} \nabla \cdot \left(\frac{\nabla c}{|\nabla c|} \right) |\nabla c| \nabla c + \frac{\rho - 1}{Fr^2} \mathbf{G},$$

$$c_t + \mathbf{u} \cdot \nabla c = \frac{1}{Pe} \nabla \cdot (M(c) \nabla \mu), \tag{7}$$

$$\mu = f(c) - \epsilon^2 \Delta c. \tag{8}$$

The dimensionless parameters are the Reynolds number, $Re = \rho_* V_* L_* / \eta_*$, the Weber number, $We = \rho_* L_* V_*^2 / \sigma$, the Froude number, $Fr = V_* / \sqrt{L_* g}$, and the diffusional Peclet number, $Pe = L_* V_* / (M_* \mu_*)$.

3. The Axisymmetric Navier-Stokes Cahn-Hilliard System

In this paper, we consider only axisymmetric flows; therefore, there is no flow in the θ (azimuthal) direction, and all θ derivatives are identically zero. Therefore, we consider only two variables, r the radial direction and z the axial direction, in the two-dimensional axisymmetric domain $\Omega = \{(r, z) : 0 < r < R,\ 0 < z < H\}$. We define the fluid velocity by the vector $\mathbf{u} = (u, w)$, where $u = u(r, z)$ is the radial component of the velocity and $w = w(r, z)$ is the component in the axial direction. We use the Boussinesq approximation to represent the gravitational force due to the density difference between the jet and the ambient fluid. The governing equations for axisymmetric flow are

$$\frac{1}{r}(ru)_r + w_z = 0, \tag{9}$$

$$u_t + uu_r + wu_z = -p_r + \frac{1}{Re} \left[\frac{1}{r}(r(2\eta u_r))_r \right.$$
$$\left. +(\eta(w_r + u_z))_z - \frac{2\eta u}{r^2} \right] + F_1, \tag{10}$$

$$w_t + uw_r + ww_z = -p_z + \frac{1}{Re} \left[\frac{1}{r}(r\eta(w_r + u_z))_r \right.$$
$$\left. +(2\eta w_z)_z \right] + F_2 - \frac{\rho - 1}{Fr^2}, \tag{11}$$

$$c_t + uc_r + wc_z = \frac{1}{Pe} \left[\frac{1}{r}(rM(c)\mu_r)_r + (M(c)\mu_z)_z \right], \tag{12}$$

$$\mu = f(c) - \epsilon^2 \left[\frac{1}{r}(rc_r)_r + c_{zz} \right], \tag{13}$$

where

$$\mathbf{F} = (F_1, F_2) = -\frac{6\sqrt{2}\epsilon}{We} \nabla \cdot \left(\frac{\nabla c}{|\nabla c|} \right) |\nabla c| \nabla c,$$

and

$$\nabla c = (c_r, c_z), \qquad \nabla \cdot (\phi, \psi) = \frac{1}{r}(r\phi)_r + \psi_z,$$

with the subscript indexes t, r, and z referring to differentiation with respect to the variable.

We, next, specify the boundary conditions. The amplitude of the velocity fluctuation is adjusted such that a droplet is pinched off at the same downstream location as in the experiments. For the inflow into the nozzle, we assume time-dependent fully-developed Poissuille flow: $u(r, 2\pi, t) = 0$ and $w(r, 2\pi, t) = V_*(1 + \alpha \cos(2\pi f t))(1 - r^2)$, where α and f are the amplitude and the frequency of the velocity fluctuation, respectively. We define the Strouhal number as $St = fL_*/V_*$. Outside the nozzle, no-slip conditions are used: $u(r, 2\pi, t) = w(r, 2\pi, t) = 0$. For the axis of symmetry at $r = 0$, $u(0, z, t) = \frac{\partial w(0,z,t)}{\partial r} = 0$. For the outflow boundary at the bottom of the mesh, $z = 0$. We assume no change in the axial direction: $\frac{\partial u(r,0,t)}{\partial z} = \frac{\partial w(r,0,t)}{\partial z} = 0$.

III. THE NUMERICAL METHOD

We employ a Chorin-type projection method for the decoupling of the momentum and the continuity equations. Our strategy for solving the system, Eqs. (9)-(13), is a fractional step scheme having two parts. First, we solve the momentum and the concentration equations, Eqs. (10)-(11), without strictly enforcing the incompressibility constraint in Eqs. (9); then, we project the resulting velocity field onto the space of discretely divergence-free vector fields [8]. Then, we update the phase field in Eqs. (12) and (13). We provide a detailed description in Appendix A.

IV. NUMERICAL EXPERIMENTS

In our numerical simulations, we use the mean value for the flow rate at the nozzle. Then, the simulation follows the time evolution of the flow until the jet length

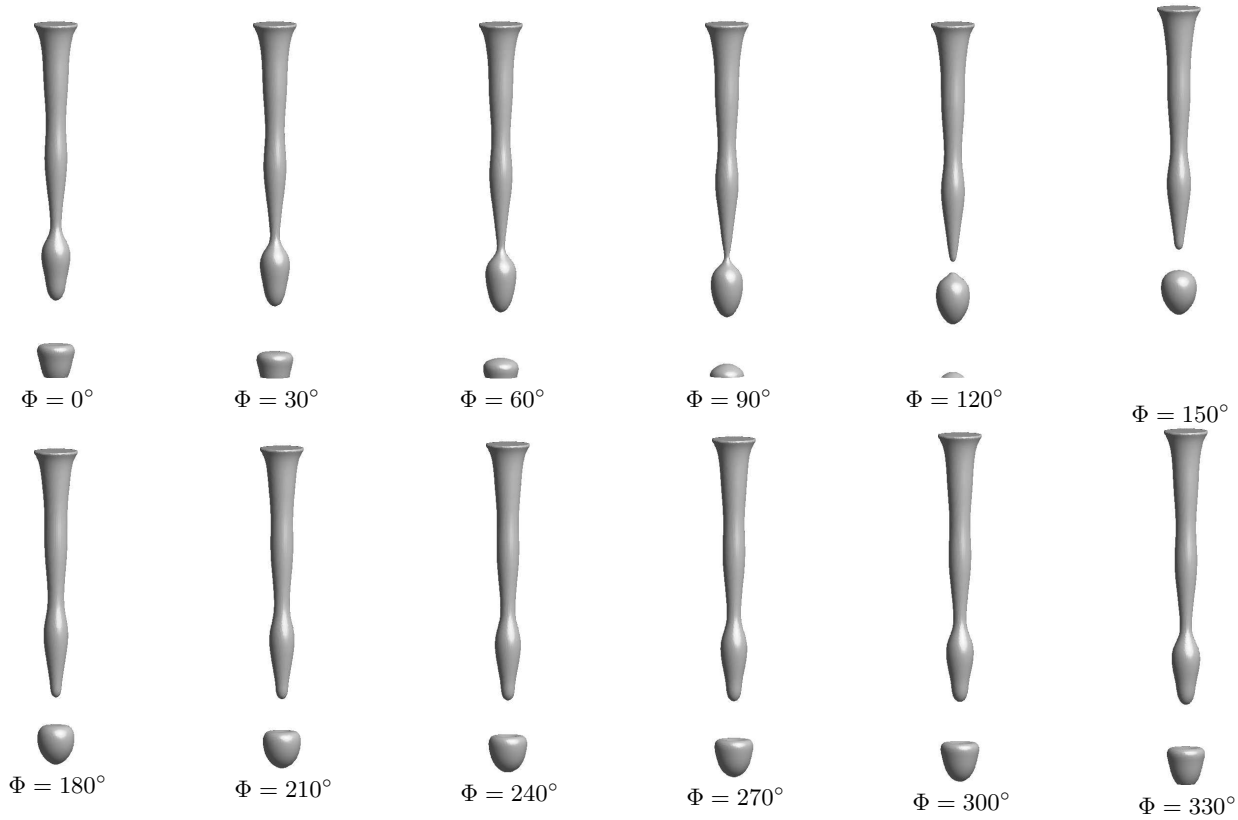

Fig. 4. Time evolution leading to multiple pinchoffs. The phase-locked sequence of jet pinchoff at $Re = 58$ and $St = 3.5$.

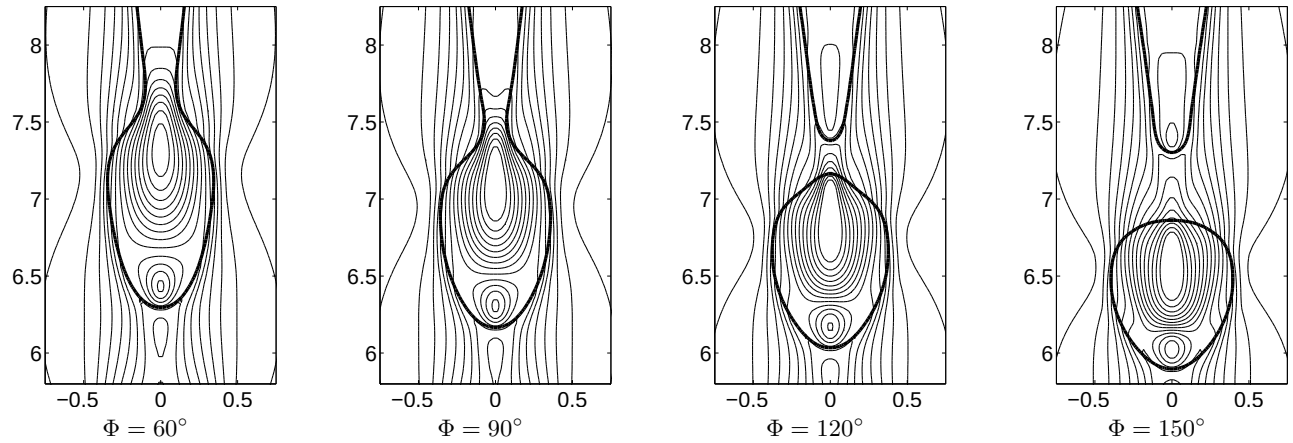

Fig. 5. Normalized axial velocity (w) contours of forced flow at $St = 3.5$ and $Re = 58$. The highest contour level is 0. Succeeding levels are decreased by 1.

versus time profile reaches a pseudo-steady behavior. The initial concentration field and velocity fields are given by

$$c^0(r,z) = 0.5\left[1 - \tanh\left(\frac{r - 0.5 - 0.05\cos(z)}{2\sqrt{2}\epsilon}\right)\right],$$
$$u^0(r,z) = w^0(r,z) = 0$$

on a domain $\Omega = \{(r,z)|0 \le r \le 0.5\pi \text{ and } 0 \le z \le 4\pi\}$. In this computation, we use the following parameters: $\epsilon = 0.02$, $Re = 58$, $We = 0.016$, $St = 3.5$, and $Pe = 100/\epsilon$.

Sequences of phase-locked images are shown in Fig. 4. We divide one cycle into 360° phases. As the liquid filament is stretched by gravity, a neck forms, elongates, and becomes thinner. In the meantime, the lower end of the filament turns into a round drop under capillary forces. The falling drop continues to stretch the thread, and eventually the Rayleigh instability leads to a pinchoff of the main drop [9].

The normalized axial velocity (w) contours of the

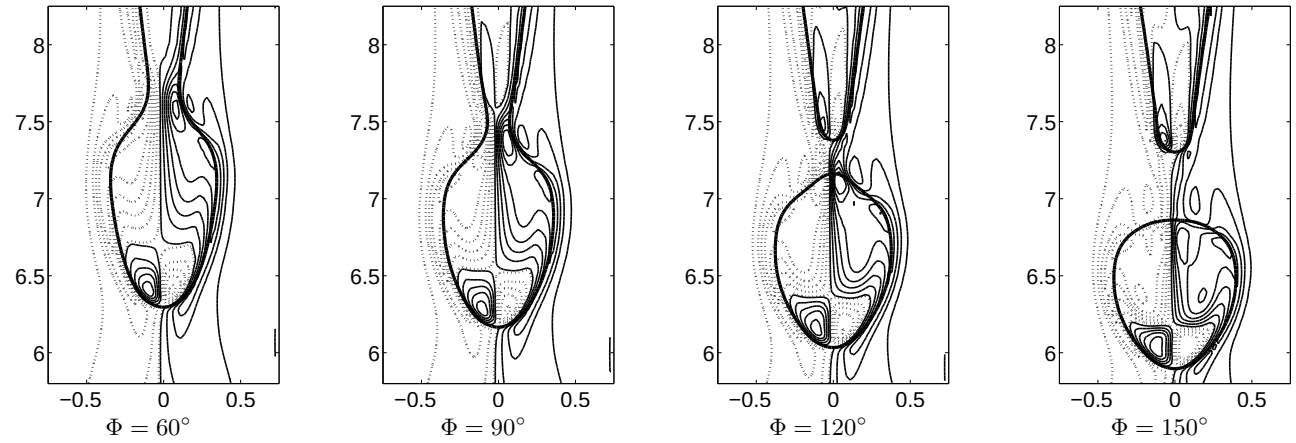

Fig. 6. Normalized vorticity field $(w_r - u_z)$ contours of forced flow at $St = 3.5$ and $Re = 58$. The solid lines represent positive vorticity. The lowest contour level is 0.05. Succeeding levels are incremented by 0.5. The dotted lines represent negative vorticity. The highest contour level is −0.05. Succeeding levels are decreased by 0.5.

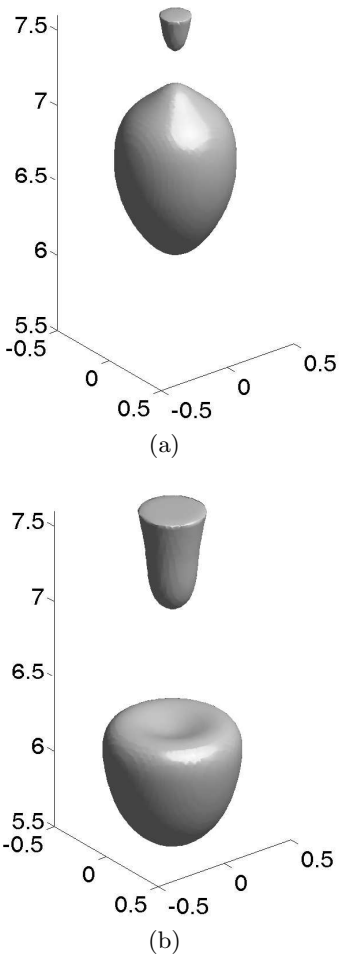

Fig. 7. (a) $\Phi = 120°$ and (b) $\Phi = 240°$.

forced flow at $St = 3.5$ and $Re = 58$ are shown in Fig. 5. The highest contour level is 0, and succeeding levels are decreased by 1. We can see that, before pinchoff ($\Phi = 60°$ and $\Phi = 90°$), the maximum axial velocity is located approximately at the jet neck. The fluid is, thus, accelerating into the neck and acting to increase the volume of the drop. After the pinchoff, the maximum velocity still resides inside the drop ($\Phi = 120°$ and $\Phi = 150°$).

The normalized vorticity field $(w_r - u_z)$ contours of the forced flow at $St = 3.5$ and $Re = 58$ are shown in Fig. 6. Solid lines represent positive vorticity. The lowest contour level is 0.05. Succeeding levels are incremented by 0.5. Dotted lines represent negative vorticity. The highest contour level is −0.05. Succeeding levels are decreased by 0.5. At the phase $\Phi = 90°$, two opposites signed vorticities develop around the jet neck and act to encourage pinchoff. A positive vorticity makes the fluid rotate clockwise while a negative vorticity makes the fluid rotate counterclockwise. After the drop pinches off, a small ring of inverted vorticity develops at the jet tip due to the recoiling interface there.

In Fig. 7, we plot close-up shapes of drops at the phases $\Phi = 120°$ and $\Phi = 240°$. At $\Phi = 120°$, after pinchoff the upstream area of the drop has a large curvature. This curvature and gravity accelerate the axial velocity, giving a maximum value at the upstream part of the drop. At $\Phi = 240°$, the upstream region of the drop has a large dimple. Interfacial tension causes the upstream surface of the drop to recover to a convex shape as the drop falls. In Fig. 8, (a) and (b) are the normalized axial velocity (w) and (c) and (d) are the vorticity field $(w_r - u_z)$ contours of forced flow. These results are qualitatively in good agreement with the experimental data [1].

V. CONCLUSIONS

In this paper, we described our numerical study of the physics of the pinchoff transition in liquid-liquid jet sys-

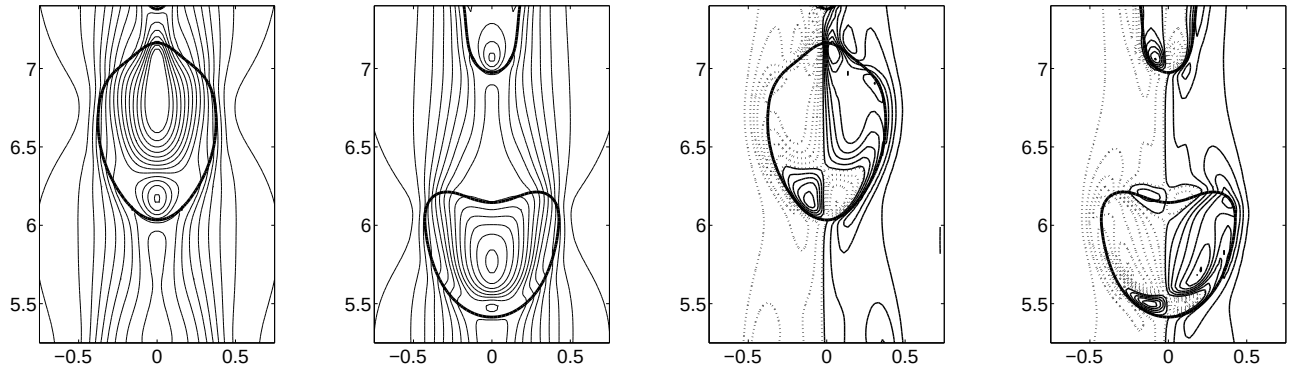

(a) $\Phi = 120°$ (b) $\Phi = 240°$ (c) $\Phi = 120°$ (d) $\Phi = 240°$

Fig. 8. (a) and (b) are the normalized axial velocity (w) and (c) and (d) are the vorticity field ($w_r - u_z$) contours of forced flow.

tems. The numerical method we used is a phase-field model for solving axisymmetric immiscible two-phase flow with variable density, viscosity, surface tension, and gravity. The phase-field model is based on a physical background. It can deal with topological transitions such as jet pinchoff. The axial velocity and vorticity structures around the jet neck before and after pinchoff are qualitatively in good agreement with the experimental results. In the future, we will include an electrostatic field in our governing equations to simulate the electrostatic ejection of liquid droplets [10].

ACKNOWLEDGMENTS

This research was supported by Basic Science Research Program through the National Research Foundation of Korea(NRF) funded by the Ministry of Education, Science and Technology (NO. R01-2008-000-20855-0). The corresponding author (J.S. Kim) was also supported by the MKE(The Ministry of Knowledge Economy), Korea, under the ITRC(Information Technology Research Center) support program supervised by the NIPA(National IT Industry Promotion Agency (NIPA-2009-2009-C1090-0902-0013). J.S. Kim thanks Professors John Lowengrub, Ellen Longmire, and Dr. Ilja Milosevic for valuable discussions and comments.

APPENDIX A: THE NUMERICAL PROCEDURE

We use a projection method for solving the system of equations, Eqs. (9)-(13) [8]. The computational grid consists of square cells of size h; these cells Ω_{ik} are centered at $(r_i = (i-0.5)h,\ z_k = (k-0.5)h)$, where $i = 1, \cdots, M$ and $k = 1, \cdots, N$. The discrete velocity field $\mathbf{u}_{ik}^n$ and the concentration field c_{ik}^n are located at the cell centers. The pressure $p_{i+\frac{1}{2},k+\frac{1}{2}}^{n-\frac{1}{2}}$ is located at the cell corners. The notation $\mathbf{u}_{ik}^n$ is used to represent an approximation to $\mathbf{u}(r_i, z_k, t^n)$, where $t^n = n\Delta t$ with Δt being a time step. Given $\mathbf{u}^{n-1}, \mathbf{u}^n,\ c^{n-1}, c^n,$ and $p^{n-\frac{1}{2}}$, we want to find $\mathbf{u}^{n+1},\ c^{n+1},$ and $p^{n+\frac{1}{2}}$, which solve the following equations of motion:

$$\nabla_d \cdot \mathbf{u}^{n+1} = 0,$$

$$\frac{\mathbf{u}^{n+1} - \mathbf{u}^n}{\Delta t} = -\nabla_d p^{n+\frac{1}{2}} + \frac{1}{2Re}\nabla_d \cdot \eta(c^{n+1}) \times[\nabla_d \mathbf{u}^{n+1} + (\nabla_d \mathbf{u}^{n+1})^T] + \frac{1}{2Re}\nabla_d \cdot \eta(c^n)[\nabla_d \mathbf{u}^n + (\nabla_d \mathbf{u}^n)^T] + \mathbf{F}^{n+\frac{1}{2}} - (\mathbf{u}\cdot\nabla_d \mathbf{u})^{n+\frac{1}{2}},$$

$$\frac{c^{n+1} - c^n}{\Delta t} = \frac{1}{Pe}\nabla_d \cdot (M(c^{n+\frac{1}{2}})\nabla_d \mu^{n+\frac{1}{2}}) - (\mathbf{u}\cdot\nabla_d c)^{n+\frac{1}{2}}, \quad \text{(A1)}$$

$$\mu^{n+\frac{1}{2}} = \frac{1}{2}[f(c^n) + f(c^{n+1})] - \frac{\epsilon^2}{2}\Delta_d(c^n + c^{n+1}). \quad \text{(A2)}$$

An outline of the main procedures in one time step of each follows:

Procedure 1. Initialize c^0 to be the locally equilibrated concentration profile and $\mathbf{u}^0$ to be the divergence-free velocity field.

Procedure 2. Update the concentration field c^n to c^{n+1}. The details of this step are presented in Section A 1 below.

Procedure 3. Compute $(\mathbf{u}\cdot\nabla_d \mathbf{u})^{n+\frac{1}{2}}$ by using a second-order ENO (essentially non-oscillatory) scheme. The half-time value $\mathbf{u}_{ik}^{n+\frac{1}{2}}$ is calculated using an extrapolation from previous values. We obtain cell-edged values as $\mathbf{u}_{i+\frac{1}{2},k}^{n+\frac{1}{2}} = (r_i \mathbf{u}_{ik}^{n+\frac{1}{2}} + r_{i+1}\mathbf{u}_{i+1,k}^{n+\frac{1}{2}})/(2r_{i+\frac{1}{2}})$ and $\mathbf{u}_{i,k+\frac{1}{2}}^{n+\frac{1}{2}} = (\mathbf{u}_{ik}^{n+\frac{1}{2}} + \mathbf{u}_{i,k+1}^{n+\frac{1}{2}})/2$. In general, the normal velocities $u_{i+\frac{1}{2},k}^{n+\frac{1}{2}}$ and $w_{i,k+\frac{1}{2}}^{n+\frac{1}{2}}$ at the edges are not divergence-free. We apply a MAC projection [11] before constructing the

convective derivatives. The equation

$$\Delta_d \phi = \nabla_{MAC} \cdot \mathbf{u}^{n+\frac{1}{2}} \tag{A3}$$

is solved for a cell-centered ϕ. We solve the resulting linear system, Eq. (A3), by using a multigrid method with a Gauss-Seidel relaxation. Then, the divergence-free normal velocities $\tilde{u}$ and $\tilde{w}$ are defined by

$$\tilde{u}^{n+\frac{1}{2}}_{i+\frac{1}{2},k} = u^{n+\frac{1}{2}}_{i+\frac{1}{2},k} - \frac{\phi_{i+1,k} - \phi_{ik}}{h},$$
$$\tilde{w}^{n+\frac{1}{2}}_{i,k+\frac{1}{2}} = w^{n+\frac{1}{2}}_{i,k+\frac{1}{2}} - \frac{\phi_{i,k+1} - \phi_{ik}}{h}.$$

The convective terms are discretized as

$$(\mathbf{u}\cdot\nabla_d \mathbf{u})^{n+\frac{1}{2}}_{ik} = \frac{r_{i+\frac{1}{2}}\tilde{u}_{i+\frac{1}{2},k} + r_{i-\frac{1}{2}}\tilde{u}_{i-\frac{1}{2},k}}{2r_i h} \times(\bar{\mathbf{u}}_{i+\frac{1}{2},k} - \bar{\mathbf{u}}_{i-\frac{1}{2},k}) + \frac{\tilde{w}_{i,k+\frac{1}{2}} + \tilde{w}_{i,k-\frac{1}{2}}}{2h}(\bar{\mathbf{u}}_{i,k+\frac{1}{2}} - \bar{\mathbf{u}}_{i,k-\frac{1}{2}}),$$

where we suppress the $n+\frac{1}{2}$ temporal index. The edge values $\bar{\mathbf{u}}^{n+\frac{1}{2}}_{i\pm\frac{1}{2},k}$ and $\bar{\mathbf{u}}^{n+\frac{1}{2}}_{i,k\pm\frac{1}{2}}$ are computed using a higher-order ENO procedure derived in Ref. 12. The procedure for computing the quantity $f_{i+\frac{1}{2},k}$ is

$$j = \begin{cases} i & \tilde{u}_{i+\frac{1}{2},k} \geq 0 \\ i+1 & \text{otherwise,} \end{cases}$$
$$a = \frac{f_{jk} - f_{j-1,k}}{h}, \quad b = \frac{f_{j+1,k} - f_{jk}}{h},$$
$$d = \begin{cases} a & \text{if } |a| \leq |b| \\ b & \text{otherwise,} \end{cases}$$
$$f_{i+\frac{1}{2},k} = f_{jk} + \frac{h}{2}d(1-2(j-i)).$$

Procedure 4. We solve

$$\frac{\mathbf{u}^* - \mathbf{u}^n}{\Delta t} = -\nabla_d p^{n-\frac{1}{2}} + \frac{1}{2Re}\nabla_d \cdot \eta(c^{n+1}) \times[\nabla_d \mathbf{u}^* + (\nabla_d \mathbf{u}^*)^T] + \frac{1}{2Re}\nabla_d \cdot \eta(c^n)[\nabla_d \mathbf{u}^n + (\nabla_d \mathbf{u}^n)^T] + \mathbf{F}^{n+\frac{1}{2}} - (\mathbf{u}\cdot\nabla_d \mathbf{u})^{n+\frac{1}{2}} \tag{A4}$$

by using a multigrid method for the intermediate velocity $\mathbf{u}^*$. Here, we use the following discretizations for the derivatives:

$$(\nabla_d p)_{ik} = \begin{pmatrix} \frac{p_{i+\frac{1}{2},k+\frac{1}{2}} + p_{i+\frac{1}{2},k-\frac{1}{2}} - p_{i-\frac{1}{2},k+\frac{1}{2}} - p_{i-\frac{1}{2},k-\frac{1}{2}}}{2h} \\ \frac{p_{i+\frac{1}{2},k+\frac{1}{2}} + p_{i-\frac{1}{2},k+\frac{1}{2}} - p_{i+\frac{1}{2},k-\frac{1}{2}} - p_{i-\frac{1}{2},k-\frac{1}{2}}}{2h} \end{pmatrix},$$
$$(\mathcal{L}^1, \mathcal{L}^2) = \nabla\cdot[\eta(\nabla\mathbf{u} + \nabla\mathbf{u}^T)] = \begin{pmatrix} \frac{2}{r}(r\eta u_r)_r - \frac{2\eta}{r^2}u + (\eta u_z)_z + (\eta w_r)_z \\ \frac{1}{r}(r\eta u_z)_r + \frac{1}{r}(r\eta w_r)_r + 2(\eta w_z)_z \end{pmatrix}.$$

Then, the first component of the viscous terms is discretized as follows:

$$\mathcal{L}^1_{ik} = \frac{2r_{i+\frac{1}{2}}\eta_{i+\frac{1}{2},k}(u_{i+1,k} - u_{ik}) - 2r_{i-\frac{1}{2}}\eta_{i-\frac{1}{2},k}(u_{ik} - u_{i-1,k})}{r_i h^2} - \frac{2\eta_{ik}}{r_i^2}u_{ik} + \frac{\eta_{i,k+\frac{1}{2}}(u_{i,k+1} - u_{ik}) - \eta_{i,k-\frac{1}{2}}(u_{ik} - u_{i,k-1})}{h^2} + \frac{\eta_{i,k+\frac{1}{2}}(w_{i+1,k+1} - w_{i-1,k+1} + w_{i+1,k} - w_{i-1,k})}{4h^2} - \frac{\eta_{i,k-\frac{1}{2}}(w_{i+1,k} - w_{i-1,k} + w_{i+1,k-1} - w_{i-1,k-1})}{4h^2},$$

where $r_{i+\frac{1}{2}} = (r_{i+1} + r_i)/2$ and $\eta_{i+\frac{1}{2},k} = [\eta(c_{ik}) + \eta(c_{i+1,k})]/2$. Next, we derive a discretization for the surface force term. The vertex-centered normal vector at the top right vertex of cell Ω_{ik} is given by

$$\mathbf{m}_{i+\frac{1}{2},k+\frac{1}{2}} = (m^r_{i+\frac{1}{2},k+\frac{1}{2}}, m^z_{i+\frac{1}{2},k+\frac{1}{2}}) = \left(\frac{c_{i+1,k} + c_{i+1,k+1} - c_{ik} - c_{i,k+1}}{2h}, \frac{c_{i,k+1} + c_{i+1,k+1} - c_{ik} - c_{i+1,k}}{2h}\right).$$

The curvature is calculated at the cell centers from the vertex-centered normals and is given by

$$\kappa(c_{ik}) = \nabla_d \cdot \left(\frac{\mathbf{m}}{|\mathbf{m}|}\right)_{ik} = \frac{1}{2h}\left(\frac{\frac{r_{i+\frac{1}{2}}}{r_i}m^r_{i+\frac{1}{2},k+\frac{1}{2}} + m^z_{i+\frac{1}{2},k+\frac{1}{2}}}{|\mathbf{m}_{i+\frac{1}{2},k+\frac{1}{2}}|} + \frac{\frac{r_{i+\frac{1}{2}}}{r_i}m^r_{i+\frac{1}{2},k-\frac{1}{2}} - m^z_{i+\frac{1}{2},k-\frac{1}{2}}}{|\mathbf{m}_{i+\frac{1}{2},k-\frac{1}{2}}|}\right.$$

$$-\frac{\frac{r_{i-\frac{1}{2}}}{r_i}m^r_{i-\frac{1}{2},k+\frac{1}{2}}-m^z_{i-\frac{1}{2},k+\frac{1}{2}}}{|\mathbf{m}_{i-\frac{1}{2},k+\frac{1}{2}}|} -\frac{\frac{r_{i-\frac{1}{2}}}{r_i}m^r_{i-\frac{1}{2},k-\frac{1}{2}}+m^z_{i-\frac{1}{2},k-\frac{1}{2}}}{|\mathbf{m}_{i-\frac{1}{2},k-\frac{1}{2}}|}\Bigg).$$

The cell-centered normal is the average of the vertex normals,

$$\nabla_d c_{ik}=\Big(\mathbf{m}_{i+\frac{1}{2},k+\frac{1}{2}}+\mathbf{m}_{i+\frac{1}{2},k-\frac{1}{2}} +\mathbf{m}_{i-\frac{1}{2},k+\frac{1}{2}}+\mathbf{m}_{i-\frac{1}{2},k-\frac{1}{2}}\Big)/4.$$

Therefore, the discretization of the surface tension force formulation $\mathbf{F}$ is

$$\mathbf{F}(c_{ik})=-6\sqrt{2}\sigma\epsilon\nabla_d\cdot\left(\frac{\mathbf{m}}{|\mathbf{m}|}\right)_{ik}|\nabla_d c_{ik}|\nabla_d c_{ik}.$$

Procedure 5. Project $\mathbf{u}^*$ onto the space of discretely divergence-free vector fields and get the velocity $\mathbf{u}^{n+1}$, *i.e.*, $\mathbf{u}^*=\mathbf{u}^{n+1}+\Delta t\nabla_d\phi$, where ϕ satisfies $\Delta_d\phi=\nabla_d\cdot\frac{\mathbf{u}^*-\mathbf{u}^n}{\Delta t}$.

Procedure 6. Update the pressure field, $p^{n+\frac{1}{2}}=p^{n-\frac{1}{2}}+\phi$. These steps complete one time step.

1. The Numerical Solution of the Axisymmetric Cahn-Hilliard Equation

We use a nonlinear full approximation storage (FAS) multigrid method [13–15] to solve the nonlinear discrete system at the implicit time level. Let us rewrite Eqs. (A1) and (A2) as follows:

$$NSO(c^{n+1},\mu^{n+\frac{1}{2}})=(\phi^n,\psi^n),$$

where

$$NSO(c^{n+1},\mu^{n+\frac{1}{2}}) =\left(\frac{c^{n+1}}{\Delta t}-\frac{1}{Pe}\nabla_d\cdot(M(c)^{n+\frac{1}{2}}\nabla_d\mu^{n+\frac{1}{2}}), \mu^{n+\frac{1}{2}}-\frac{1}{2}f(c^{n+1})+\frac{\epsilon^2}{2}\Delta_d c^{n+1}\right).$$

The source term is $(\phi^n,\ \psi^n)=(\frac{c^n}{\Delta t}+s^{n+\frac{1}{2}},\ \frac{1}{2}f(c^n)-\frac{\epsilon^2}{2}\Delta_d c^n)$, where $s^{n+\frac{1}{2}}=-(\mathbf{u}\cdot\nabla_d c)^{n+\frac{1}{2}}$. We assume a sequence of grids Ω_l (Ω_{l-1} to be coarser than Ω_l by a factor of 2).

The FAS multigrid cycle

$$\{c_l^{m+1},\mu_l^{m+\frac{1}{2}}\}=FAScycle(l,c_l^n,c_l^m,\mu_l^{m-\frac{1}{2}}, NSO_l,\phi_l^n,\psi_l^n,\nu).$$

Step I. Presmoothing

Compute $\{\bar{c}_l^m,\ \bar{\mu}_l^{m-\frac{1}{2}}\}$ by applying ν smoothing steps to $\{c_l^m,\ \mu_l^{m-\frac{1}{2}}\}$

$$\{\bar{c}_l^m,\ \bar{\mu}_l^{m-\frac{1}{2}}\}=SMOOTH^\nu(c_l^n,c_l^m,\mu_l^{m-\frac{1}{2}}, NSO_l,\phi_l^n,\psi_l^n).$$

One $SMOOTH$ relaxation operator step consists of solving the system of Eqs. (A7) and (A8) given below by using a 2×2 matrix inversion for each i and k. Let us discretize Eq. (A1) to get a smooth operator:

$$\begin{aligned}&\frac{c_{ik}^{n+1}}{\Delta t}+\left(\frac{r_{i+\frac{1}{2}}M^{n+\frac{1}{2}}_{i+\frac{1}{2},k}+r_{i-\frac{1}{2}}M^{n+\frac{1}{2}}_{i-\frac{1}{2},k}}{r_i h^2 Pe} +\frac{M^{n+\frac{1}{2}}_{i,k+\frac{1}{2}}+M^{n+\frac{1}{2}}_{i,k-\frac{1}{2}}}{h^2Pe}\right)\mu_{ik}^{n+\frac{1}{2}}\\ &=\frac{c_{ik}^n}{\Delta t}+s_{ik}^{n+\frac{1}{2}} +\frac{r_{i+\frac{1}{2}}M^{n+\frac{1}{2}}_{i+\frac{1}{2},k}\mu^{n+\frac{1}{2}}_{i+1,k}+r_{i-\frac{1}{2}}M^{n+\frac{1}{2}}_{i-\frac{1}{2},k}\mu^{n+\frac{1}{2}}_{i-1,k}}{r_i h^2 Pe}\\ &+\frac{M^{n+\frac{1}{2}}_{i,k+\frac{1}{2}}\mu^{n+\frac{1}{2}}_{i,k+1}+M^{n+\frac{1}{2}}_{i,k-\frac{1}{2}}\mu^{n+\frac{1}{2}}_{i,k-1}}{h^2Pe},\end{aligned}\tag{A5}$$

where $M^{n+\frac{1}{2}}_{i+\frac{1}{2},k}=M((c^{n+1}_{ik}+c^{n+1}_{i+1,k}+c^n_{ik}+c^n_{i+1,k})/4)$. Next, let us discretize Eq. (A2). Since $f(c_{ik}^{n+1})$ is nonlinear with respect to c_{ik}^{n+1}, we linearize $f(c_{ik}^{n+1})$ at c_{ik}^m, *i.e.*, $f(c_{ik}^{n+1})\approx f(c_{ik}^m)+\frac{df(c_{ik}^m)}{dc}(c_{ik}^{n+1}-c_{ik}^m)$. After substitution of this into Eq. (A2) and rearranging the terms, we get

$$\begin{aligned}&-\left(\frac{df(c_{ik}^m)}{2dc}+\frac{2\epsilon^2}{h^2}\right)c_{ik}^{n+1}+\mu_{ik}^{n+\frac{1}{2}}\\ &=\frac{1}{2}f(c_{ik}^n)-\frac{\epsilon^2}{2}\Delta_d c_{ik}^n+\frac{1}{2}f(c_{ik}^m)\end{aligned}\tag{A6}$$

$$-\frac{df(c_{ik}^m)}{2dc}c_{ik}^m-\frac{\epsilon^2}{2}\left(\frac{r_{i+\frac{1}{2}}c^m_{i+1,k}+r_{i-\frac{1}{2}}c^{n+1}_{i-1,k}}{r_i h^2} +\frac{c^m_{i,k+1}+c^{n+1}_{i,k-1}}{h^2}\right).$$

Next, we replace c_{jl}^{n+1} and $\mu_{jl}^{n+\frac{1}{2}}$ in Eqs. (A5) and (A6) with $\bar{c}_{jl}^m$ and $\bar{\mu}_{jl}^{m-\frac{1}{2}}$ if $(j<i)$ or $(j=i$ and $l\le k)$, otherwise, with c_{jl}^m and $\mu_{jl}^{m-\frac{1}{2}}$, *i.e.*,

$$\frac{\bar{c}_{ik}^m}{\Delta t}+\left(\frac{r_{i+\frac{1}{2}}M_{i+\frac{1}{2},k}^{n+\frac{1}{2}}+r_{i-\frac{1}{2}}M_{i-\frac{1}{2},k}^{n+\frac{1}{2}}}{r_i h^2 Pe}+\frac{M_{i,k+\frac{1}{2}}^{n+\frac{1}{2}}+M_{i,k-\frac{1}{2}}^{n+\frac{1}{2}}}{h^2 Pe}\right)\bar{\mu}_{ik}^{m-\frac{1}{2}}$$
$$=\frac{c_{ik}^n}{\Delta t}+s_{ik}^{n+\frac{1}{2}}+\frac{r_{i+\frac{1}{2}}M_{i+\frac{1}{2},k}^{n+\frac{1}{2}}\mu_{i+1,k}^{m-\frac{1}{2}}+r_{i-\frac{1}{2}}M_{i-\frac{1}{2},k}^{n+\frac{1}{2}}\bar{\mu}_{i-1,k}^{m-\frac{1}{2}}}{r_i h^2 Pe}+\frac{M_{i,k+\frac{1}{2}}^{n+\frac{1}{2}}\mu_{i,k+1}^{m-\frac{1}{2}}+M_{i,k-\frac{1}{2}}^{n+\frac{1}{2}}\bar{\mu}_{i,k-1}^{m-\frac{1}{2}}}{h^2 Pe}, \quad \text{(A7)}$$

$$-\left(\frac{df(c_{ik}^m)}{2dc}+\frac{2\epsilon^2}{h^2}\right)\bar{c}_{ik}^m+\bar{\mu}_{ik}^{m-\frac{1}{2}}=\frac{1}{2}f(c_{ik}^n)-\frac{\epsilon^2}{2}\Delta_d c_{ik}^n+\frac{1}{2}f(c_{ik}^m) \quad \text{(A8)}$$

$$-\frac{df(c_{ik}^m)}{2dc}c_{ik}^m-\frac{\epsilon^2}{2}\left(\frac{r_{i+\frac{1}{2}}c_{i+1,k}^m+r_{i-\frac{1}{2}}\bar{c}_{i-1,k}^m}{r_i h^2}+\frac{c_{i,k+1}^m+\bar{c}_{i,k-1}^m}{h^2}\right).$$

Step II. Compute the defect: $(\bar{d_1}_l^{\,m},\bar{d_2}_l^{\,m})=(\phi_l^n,\psi_l^n)-NSO_l(\bar{c}_l^n,\bar{c}_l^m,\bar{\mu}_l^{m-\frac{1}{2}})$.

• Restrict the defect and $\{\bar{c}_l^m,\ \bar{\mu}_l^{m-\frac{1}{2}}\}$:

$$(\bar{d_1}_{l-1}^{\,m},\bar{d_2}_{l-1}^{\,m})=I_l^{l-1}(\bar{d_1}_l^{\,m},\bar{d_2}_l^{\,m}),$$
$$(\bar{c}_{l-1}^m,\bar{\mu}_{l-1}^{m-\frac{1}{2}})=I_l^{l-1}(\bar{c}_l^m,\bar{\mu}_l^{m-\frac{1}{2}}).$$

The restriction operator I_l^{l-1} maps l-level functions to $(l-1)$-level functions:

$$c_{l-1}(r_i,z_k)=I_l^{l-1}c_l(r_i,z_k)=\frac{1}{4h^2 r_i}\int_{z_{k-1}}^{z_{k+1}}\int_{r_{i-1}}^{r_{i+1}}c(r,z)r\,dr\,dz$$
$$=[r_{i-\frac{1}{2}}(c_{i-\frac{1}{2},k-\frac{1}{2}}+c_{i-\frac{1}{2},k+\frac{1}{2}})+r_{i+\frac{1}{2}}(c_{i+\frac{1}{2},k-\frac{1}{2}}+c_{i+\frac{1}{2},k+\frac{1}{2}})]/(4r_i)$$

• Compute the right-hand side:

$$(\phi_{l-1}^n,\psi_{l-1}^n)=(\bar{d_1}_{l-1}^{\,m},\bar{d_2}_{l-1}^{\,m})+NSO_{l-1}(\bar{c}_{l-1}^n,\bar{c}_{l-1}^m,\bar{\mu}_{l-1}^{m-\frac{1}{2}}).$$

• Compute an approximate solution $\{\hat{c}_{l-1}^m,\ \hat{\mu}_{l-1}^{m-\frac{1}{2}}\}$ of the coarse grid equation on Ω_{l-1}, *i.e.*

$$NSO_{l-1}(c_{l-1}^n,c_{l-1}^m,\mu_{l-1}^{m-\frac{1}{2}})=(\phi_{l-1}^n,\psi_{l-1}^n). \quad \text{(A9)}$$

If $l=1$, we employ smoothing steps. If $l>1$, we solve Eq. (A9) by performing a FAS l-grid cycle using $\{\bar{c}_{l-1}^m,\ \bar{\mu}_{l-1}^{m-\frac{1}{2}}\}$ as an initial approximation:

$$\{\hat{c}_{l-1}^m,\hat{\mu}_{l-1}^{m-\frac{1}{2}}\}=\text{FAScycle}(l-1,c_{l-1}^n,\bar{c}_{l-1}^m,\bar{\mu}_{l-1}^{m-\frac{1}{2}},NSO_{l-1},\phi_{l-1}^n,\psi_{l-1}^n,\nu).$$

• Compute the coarse grid correction (CGC):

$$\hat{v}_{1l-1}^m=\hat{c}_{l-1}^m-\bar{c}_{l-1}^m,\quad \hat{v}_{2l-1}^{m-\frac{1}{2}}=\hat{\mu}_{l-1}^{m-\frac{1}{2}}-\bar{\mu}_{l-1}^{m-\frac{1}{2}}.$$

• Interpolate the correction: $\hat{v}_{1l}^m=I_{l-1}^l\hat{v}_{1l-1}^m,\quad \hat{v}_{2l}^{m-\frac{1}{2}}=I_{l-1}^l\hat{v}_{2l-1}^{m-\frac{1}{2}}$. The interpolation operator I_{l-1}^l maps $(l-1)$-level functions to l-level functions. Then, the prolongation operator I_{l-1}^l from Ω_{l-1} to Ω_l is defined by

$$\begin{pmatrix}v_l(r_{i-\frac{1}{2}},z_{k-\frac{1}{2}})\\ v_l(r_{i-\frac{1}{2}},z_{k+\frac{1}{2}})\\ v_l(r_{i+\frac{1}{2}},z_{k-\frac{1}{2}})\\ v_l(r_{i+\frac{1}{2}},z_{k+\frac{1}{2}})\end{pmatrix}=v_{l-1}(r_i,z_k)\begin{pmatrix}\frac{r_i}{r_{i-\frac{1}{2}}}\\ \frac{r_i}{r_{i-\frac{1}{2}}}\\ \frac{r_i}{r_{i+\frac{1}{2}}}\\ \frac{r_i}{r_{i+\frac{1}{2}}}\end{pmatrix}.$$

• Compute the corrected approximation on Ω_l:

$$c_l^{m,\text{ after }CGC}=\bar{c}_l^m+\hat{v_{1l}}^m,$$
$$\mu_l^{m-\frac{1}{2},\text{ after }CGC}=\bar{\mu}_l^{m-\frac{1}{2}}+\hat{v_{2l}}^{m-\frac{1}{2}}.$$

Step III. Postsmoothing: Compute $\{c_l^{m+1},\mu_l^{m+\frac{1}{2}}\}$ by applying ν smoothing steps to $c_l^{m,\text{ after }CGC}$, $\mu_l^{m-\frac{1}{2},\text{ after }CGC}$.

$$\{c_l^{m+1},\mu_l^{m+\frac{1}{2}}\}=SMOOTH^\nu(c_l^n,c_l^{m,\text{ after }CGC},\mu_l^{m-\frac{1}{2},\text{ after }CGC},NSO_l,\phi_l^n,\psi_l^n).$$

This completes the description of a nonlinear FAScycle for the axisymmetric Cahn-Hilliard equation.

REFERENCES

[1] I. N. Milosevic and E. K. Longmire, Int. J. Multiphase Flow **28**, 1853 (2002).
[2] J. S. Lowengrub and L. Truskinovsky, Proc. R. Soc. Lond. A **454**, 2617 (1998).
[3] J. S. Maeng, K. S. Yoo, S. Song and S. Heu, J. Korean Phys. Soc. **48**, 902 (2006).
[4] S. J. An, Y. D. Kim, S. Heu and J. S. Maeng, J. Korean Phys. Soc. **49**, 651 (2006).
[5] R. Zhang, X. He and S. Chen, Comput. Phys. Commun. **129**, 121 (2000).
[6] D. M. Anderson, G. B. McFadden and A. A. Wheeler, Ann. Rev. Fluid Mech. **30**, 139 (1998).
[7] J. S. Kim, J. Comput. Phys. **204**, 784 (2005).
[8] J. B. Bell, P. Collela and H. M. Glaz, J. Comput. Phys. **85**, 257 (1989).

[9] X. Yang, J. J. Feng, C. Liu and J. Shen, J. Comput. Phys. **218**, 417 (2006).
[10] Y. J. Kim, H. S. Ko, S. H. Lee, S. U. Son, D. W. Jung and D. Y. Byun, J. Korean Phys. Soc. **51**, S42 (2007).
[11] M. Sussman and E. G. Puckett, J. Comput. Phys. **162**, 301 (2000).
[12] C. W. Shu and S. Osher, J. Comput. Phys. **83**, 32 (1989).
[13] J. S. Kim and H. O. Bae, J. Korean Phys. Soc. **53**, 672 (2008).
[14] J. S. Kim, J. Korean Phys. Soc. **49**, 1903 (2006).
[15] U. Trottenberg, C. Oosterlee and A. Schüller, *MULTI-GRID* (Academic Press, London, 2001).